Electronic Supplementary Information (ESI)

The following results are given in ESI.
(1) UV−visible diffuse reflection spectra [**S1**]
(2) Typical TRESR spectrum of the single crystal of Py/PMDA [**S2**]
(3) X-ray crystallographic data of Py/DMPI and Py/PMDA [**S3**, **S4**]
(4) Results of the molecular orbital calculations using Gaussian 09 (transition energies, oscillator strengths, and orbital energies of Py/DMPI and Py/PMDA and hyperfine splitting pattern of the cation radical of pyrene (Py+) and the anion radical of DMPI (DMPI^{-}) and estimation of the magnitude of the effective isotropic hyperfine coupling [**S5**– **S7**]
(5) Estimation of the fine-structure parameters using ORCA program package [**S8**]
(6) Typical MC of the VVB Film of Py/PMDA [**S9**]
(7) Detail procedures of the MC effect calculation by the DD pair mechanism and the *J* and *k* dependences [**S10**]
(8) Detail procedures of the MC effect calculation by the TD pair mechanism and the *J* and *k* dependences [**S11**]

S1. UV−visible diffuse reflection spectra

Fig. S1 shows the UV−visible diffuse reflection spectra of all compounds in this work (pyrene, Py/DMPI, Py/PMDA, DMPI, and PMDA). The spectra of pyrene, DMPI and PMDA were also measured and added to Fig 2(a) in the main text.

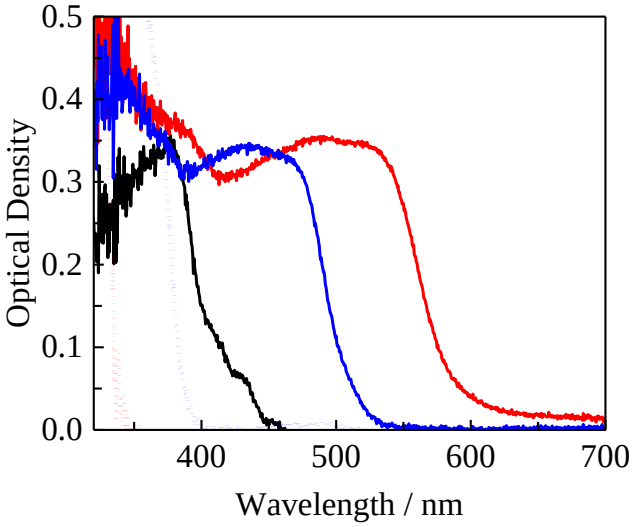

Fig.S1 UV−visible diffuse reflection spectra of pyrene (black; solid), Py/DMPI (blue; solid), Py/PMDA (red; solid) , DMPI (blue; dot), and PMDA (red; dot).

S2. Typical TRESR spectrum of the single crystal of Py/PMDA

In order to investigate that the observed triplet state is the mobile exciton or trapped one, the line shape of the single transition of TRESR was examined using the single crystal of Py/PMDA. The typical TRESR signal with a much broad line-width compared with that of Py/DMPI, was observed as given in Fig. S2. Although the signal was weak and difficult of confident judgement, Lorentzian seems to be better.

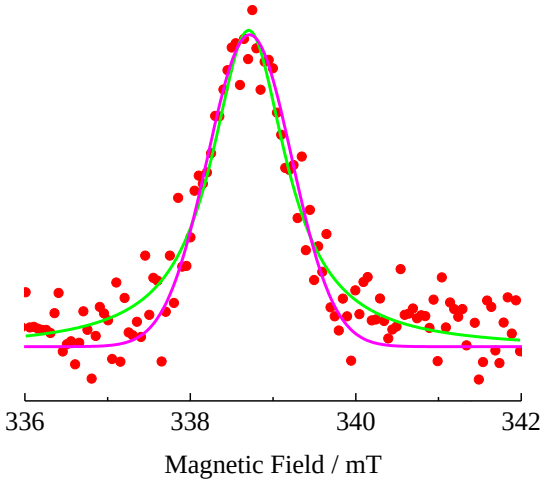

Fig.S2 Typical TRESR spectra of the single crystal of Py/PMDA (red), Lorenz fit (green) and Gaussian fit (pink).

S3. X-ray crystallographic data of Py/DMPI

Diffraction data were collected on a Rigaku AFC11 with Saturn 724+ CCD diffractometer using graphite-monochromated Mo Kα radiation (λ = 0.710747 Å). Determination of the cell parameters and collection of the reflection intensities were performed using the CrystalClear software package.[37] The structures were solved by direct methods using the program SIR97[38] and refined against *F*2 with full-matrix least squares techniques using the program SHELXL-2014/7.[39] All calculations were performed using the WinGX software package.[40] Crystal data for Py/DMPI are listed in Table S1. CCDC 1546840

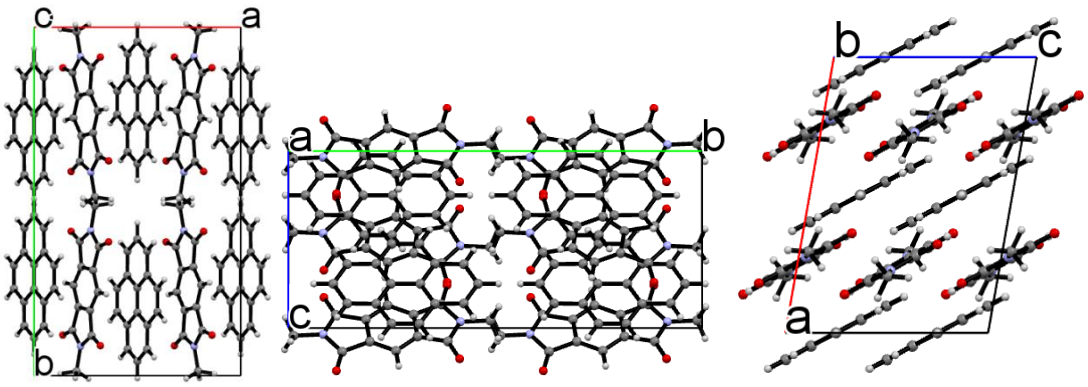

Fig.S3 *ab*-plane projection (left). *bc*-plane projection (center). *ac*-plane projection (right).

Table S1 Crystal data for Py/DMPI

Empirical formula	C28 H18 N2 O4	
Formula weight	446.44	
Temperature	200(2) K	
Wavelength	0.71075 Å	
Crystal system	Monoclinic	
Space group	C 2/c	
Unit cell dimensions	a = 12.019(6) Å	α = 90°
	b = 20.022(9) Å	β = 99.990(5)°
	c = 8.703(4) Å	γ = 90°
Volume	2062.6(16) Å^3	
Z	4	
Density(calculated)	1.438 g/cm^3	
Absorption coefficient	0.097 mm^{-1}	
Crystal size	0.200 ×0.150 ×0.100 mm^3	
R indices(all data)	R1 = 0.0532, wR2 = 0.1147	
Goodness-of-fit on F^2	1.099	

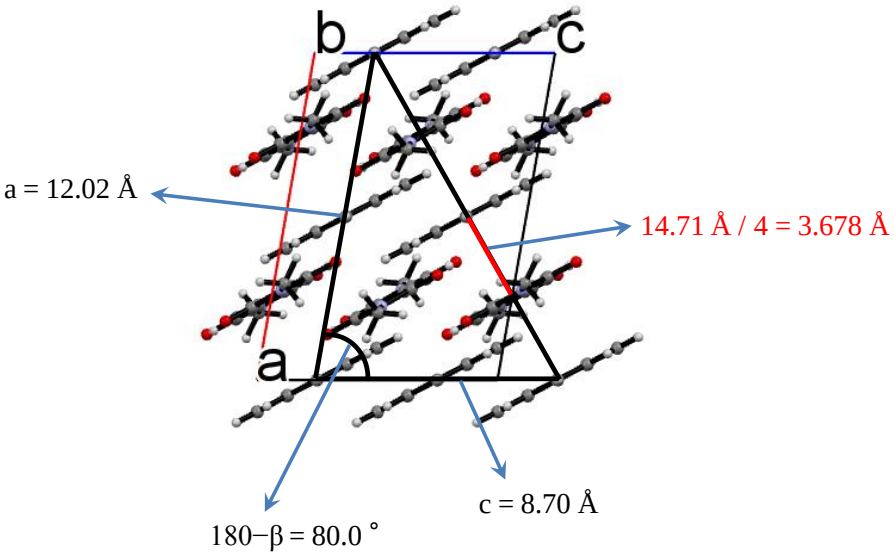

Fig.S4 The distances between pyrene and DMPI in the crystals by *ac*-plane projection

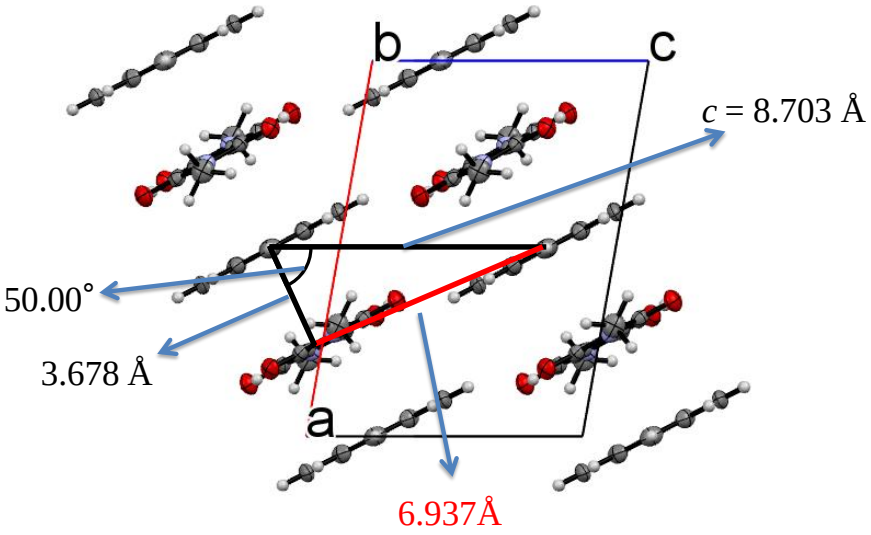

Fig.S5 The 2nd nearest distances between pyrene and DMPI in the crystals by *ac*-plane projection

S4. X-ray crystallographic data of Py/PMDA

Diffraction data collection and analyses were carried out using the same procedures described already for Py/DMPI. Crystal data for Py/PMDA are listed in Table S2. CCDC 1546841

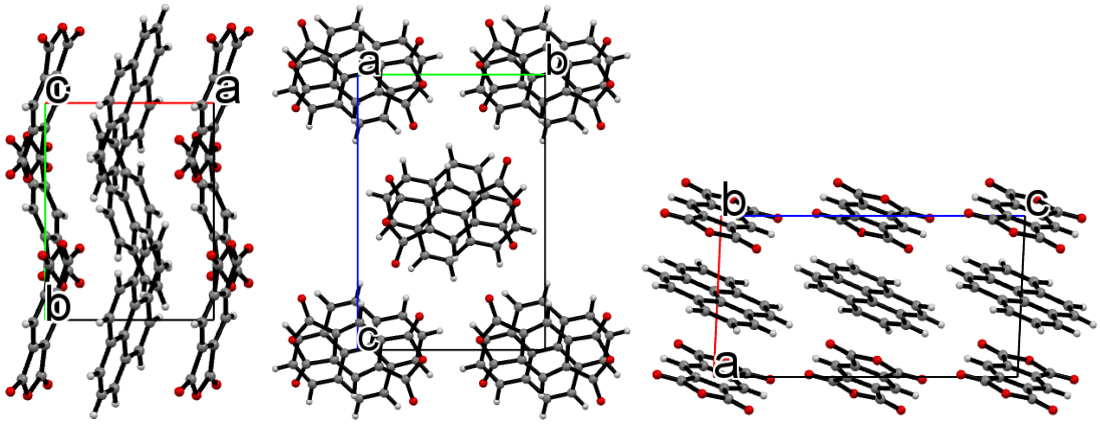

Fig.S6 *ab*-plane projection (left). *bc*-plane projection (center). *ac*-plane projection (right).

Table S2 Crystal data for Py/PMDA

Empirical formula	C26 H12 O6	
Formula weight	420.36	
Temperature	200(2) K	
Wavelength	0.71075 Å	
Crystal system	Monoclinic	
Space group	P 21/c	
Unit cell dimensions	a = 7.268(6) Å	α = 90°
	b = 9.350(7) Å	β = 92.710(11)°
	c = 13.757(11) Å	γ = 90°
Volume	933.8(12) Å^3	
Z	2	
Density(calculated)	1.495 g/cm^3	
Absorption coefficient	0.107 mm^{-1}	
Crystal size	0.130 ×0.120 ×0.090 mm^3	
R indices(all data)	R1 = 0.0566, wR2 = 0.1164	
Goodness-of-fit on F^2	1.119	

S5. Transition energies, oscillator strengths, and orbital energies obtained from the molecular orbital calculations of Py/DMPI

Transition energies and their oscillator strengths of Py/DMPI are listed in Table S3, which were obtained by using TD-DFT calculations. The one-electron molecular orbital energies are given in Table S4. Their molecular orbitals are given in Fig. S7.

Table S3 Calculated excited state of Py/DMPI crystal.

Excited State	Transition	Energy (Wavelength)	Oscillator Strength
1	HOMO → LUMO	2.2055 eV (562.16 nm)	0.0057
2	HOMO−1 → LUMO	3.0239 eV (410.02 nm)	0.0009
3	HOMO → LUMO+1 (15%) HOMO → LUMO+2 (85%)	3.3618 eV (368.80 nm)	0.0012

Table S4 Molecular orbital energy of Py/DMPI crystal.

Molecular Orbital	Energy / Hartrees	Energy / eV
LUMO+2	−0.07310	−1.9892
LUMO+1	−0.09400	−2.5579
LUMO	−0.12546	−3.4139
HOMO	−0.21283	−5.7914
HOMO−1	−0.24572	−6.6863

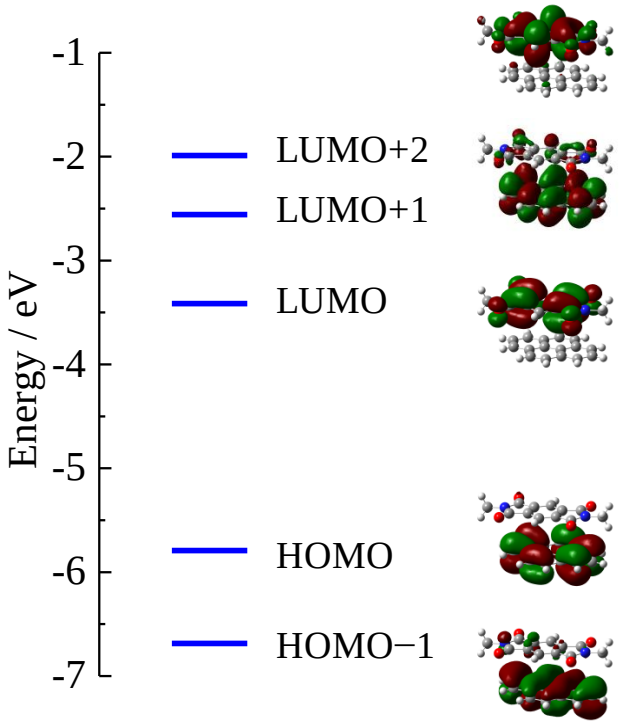

Fig.S7 Molecular orbitals and orbital energies of Py/DMPI.

S6. Transition energies, oscillator strengths, and orbital energies obtained from the molecular orbital calculations of Py/PMDA

Transition energies and their oscillator strengths of Py/DMPI are listed in Table S5, which were obtained by using TD-DFT calculations. The one-electron molecular orbital energies are given in Table S6. Their molecular orbitals are given in Fig. S8.

Table S5 Calculated excited etate of Py/PMDA crystal.

Excited State	Transition	Energy (Wavelength)	Oscillator Strength
1	HOMO → LUMO	1.8573 eV (667.57 nm)	0.0397
2	HOMO → LUMO+1	2.6074 eV (475.50 nm)	0.0004
3	HOMO−1 → LUMO	2.6571 eV (466.61 nm)	0.0108

Table S6 Molecular orbital energy of Py/PMDA crystal.

Molecular Orbital	Energy / Hartrees	Energy / eV
LUMO+2	−0.05686	−1.5472
LUMO+1	−0.06224	−1.6936
LUMO	−0.10087	−2.7448
HOMO	−0.20399	−5.5509
HOMO−1	−0.23550	−6.4082

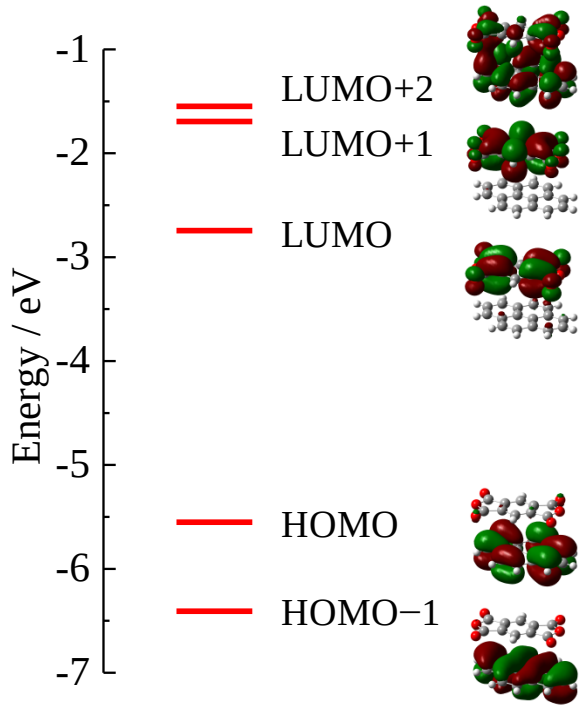

Fig.S8 Molecular orbitals and orbital energies of Py/PMDA.

S7. Calculation of hyperfine splitting pattern of the cation radical of pyrene (Py+) and the anion radical of DMPI (DMPI⁻), and estimation of the magnitude of the effective isotropic hyperfine coupling

The hyperfine couplings of the cation radical of pyrene (Py^+) and the anon radical of DMPI ($DMPI^-$) were calculated using Gaussian 09W. The calculation was performed by using DFT with the UB3LYP function 6-31G(d,p) basis sets for the optimized molecular structures. The calculated isotropic Ferimi contact couplings are listed in Table S7. The spectral splitting patterns in the frequency region were calculated as shown Fig.S9. By the weighted averaging of the split pairs based on their spectral patterns, the effective isotropic hyperfine-couplings of pyrene and DMPI were estimated to be $a_{D1}^{eff} = -30.0$ MHz and $a_{D2}^{eff} = -8.0$ MHz, respectively.

$$\sum_i \boldsymbol{S_{D1}} \cdot \boldsymbol{A_i} \cdot \boldsymbol{I_{D1i}} \rightarrow \boldsymbol{a_{D1}^{eff}} \boldsymbol{S_{D1}} \cdot \boldsymbol{I_{D1}}\,, \qquad \sum_j \boldsymbol{S_{D2}} \cdot \boldsymbol{A_j} \cdot \boldsymbol{I_{D2j}} \rightarrow \boldsymbol{a_{D2}^{eff}} \boldsymbol{S_{D2}} \cdot \boldsymbol{I_{D2}}\,. \qquad \text{(S1)}$$

Here, the signs of a_{D1}^{eff} and a_{D2}^{eff} were chosen to be negative, because the major isotropic hyperfine couplings of Py^+ and $DMPI^-$ were negative. The anisotropic terms were neglected, since their magnitude was much smaller than that of the isotropic terms.

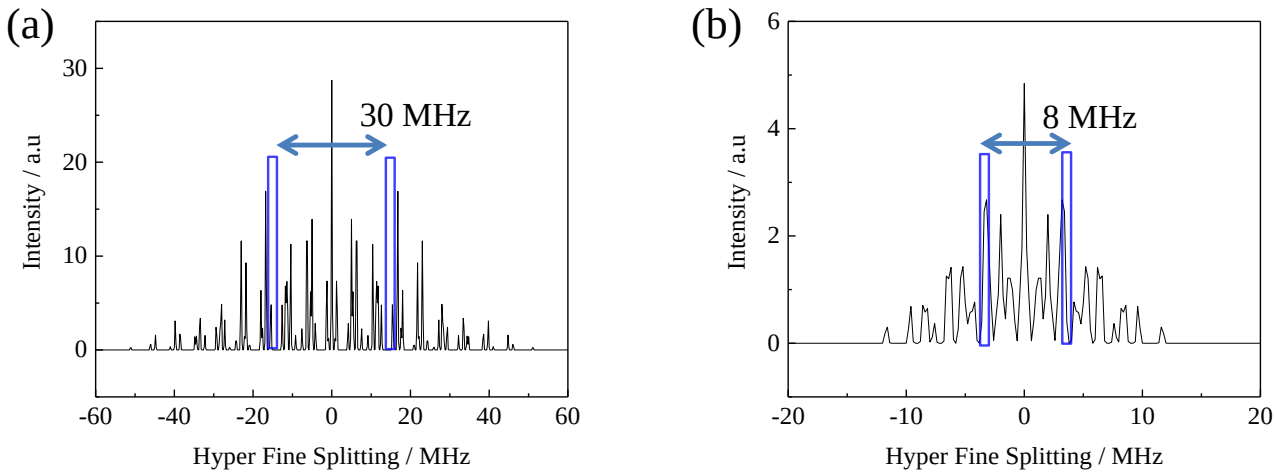

Fig.S9 The calculated hyper fine splitting pattern of (a) pyrene cation, (b) DMPI anion and their effective hyperfine coupling approximated by $\boldsymbol{a_D^{eff}} \boldsymbol{S_D} \cdot \boldsymbol{I_D}$ (S = 1/2 and I = 1/2).

Table S7 The calculated Isotropic Fermi contact couplings of pyrene cation and DMPI anion.

pyrene cation	Isotropic Fermi Contact Couplings /MHz	DMPI anion	Isotropic Fermi Contact Couplings /MHz
H(1)	-16.74237	N(14)	-3.12385
H(1)	5.02858	N(14)	-3.12385
H(1)	-16.74386	H(1)	3.40856
H(1)	-6.29519	H(1)	3.40856
H(1)	-6.29312	H(1)	-0.211
H(1)	-6.29901	H(1)	-2.01744
H(1)	-6.2957	H(1)	-2.01743
H(1)	-16.74076	H(1)	-0.211
H(1)	5.02861	H(1)	-2.01744
H(1)	-16.7453	H(1)	-2.01743

S8. Estimation of the fine-structure parameters using ORCA program package

For the *g* and fine-structure tensors, calculation were also implemented in Orca program package[42] for the optimized structure of pyrene, and for the X-ray determined structures of Py/DMPI and Py/PMDA. The calculation was performed by using DFT with the UKS B3LYP function and 6-31G basis sets for the molecular structures determined by crystallographic analyses. In ORCA package, we chose the key word, "DIRECT", for the calculation of dipolar spin-spin contribution and "QRO" for the spin-orbit calculation. The calculated fine-structure parameters (*D* and *E*) and the contributions of the spin-spin and spin-orbit interaction terms are listed in Table S8. The comparisons of the results obtained using the different methods are also shown. As shown in Table S8, the better values, which were close to the experimental data, were obtained, when the "DIRECT" for the spin-spin interaction term and "QRO" for the spin-orbit interaction term. The sign of the *D* value was positive both for the pyrene and Py/DMPI.

Table S8 The zero field splitting parameters were computed by using the ORCA program ref [42].

Pyrene	1	2	3	4	obs.[a]
DTensor DSS DSOC	SS DIRECT	SS UNO	SS and SO DIRECT QRO	SS and SO UNO QRO	
D / cm^{-1}	+0.09186	−0.05338	+0.086874	−0.06033	0.0863
E / cm^{-1}	+0.01086	−0.00415	+0.004556	−0.0098	0.0167

Py/PMDA	1	2	3	4	obs.	obs.[b](ODMR)
DTensor DSS DSOC	SS DIRECT	SS UNO	SS and SO DIRECT QRO	SS and SO UNO QRO		
D / cm^{-1}	−0.05415	−0.02000	+0.04456	−0.02955	−0.0141	0.0555
E / cm^{-1}	−0.01638	−0.002276	+0.010279	−0.00571	0	0.00883

Py/DMPI	1	2	3	4	obs.
DTensor DSS DSOC	SS DIRECT	SS UNO	SS and SO DIRECT QRO	SS and SO UNO QRO	
D / cm^{-1}	+0.068399	−0.036117	+0.069092	−0.04585	0.0830
E / cm^{-1}	+0.013349	−0.000674	+0.007121	−0.00343	0.0160

[a] ref [44], [b] ref [23,45]

S9. Typical MC of the VVB Film of Py/PMDA

To obtain some insights about carrier dynamics, we investigated the MC effect in the photocurrent for Py/PMDA. The positive MC effect (~1.3% increase at the maximum) relative to the magnetic field increase was observed in Py/PMDA VVD film as shown in Fig. S10. The MC curve of Py/PMDA was also approximately fitted like as that of Py/DMPI by triple Gaussians (narrow, middle, and broad components).

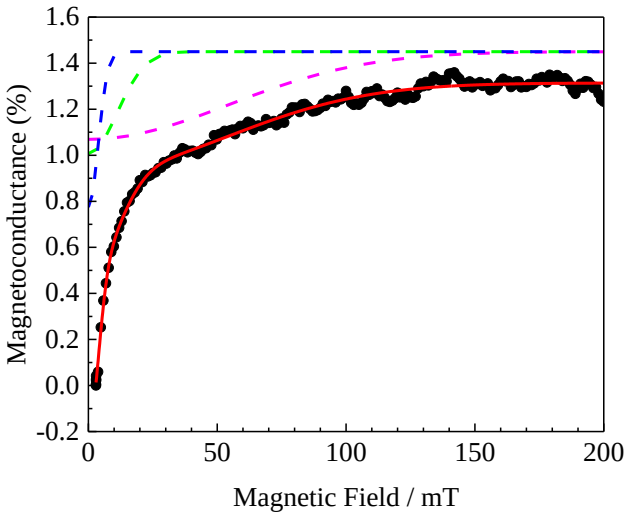

Fig.S10 MC effects in the photocurrent of VVD film of Py/PMDA. Observed curve and the fit (red curve) using triple Gaussians (blue, green, and purple broken lines).

S10. Detail procedures of the MC effect calculation by the DD pair mechanism and the *J* and *k* dependences

The kinetic models of the DD mechanism is given in Scheme S1.

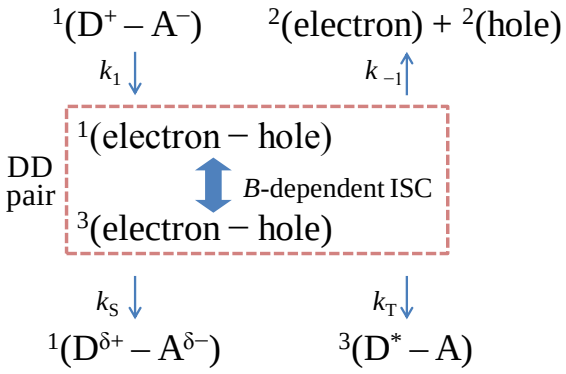

Scheme S1 A kinetic models of the DD mechanism

The rate equation of the density matrix for the DD mechanism is given by

$$\frac{\mathrm{d}\boldsymbol{\rho}_{DD}(t)}{\mathrm{d}t} = k_1\boldsymbol{\rho}_{DD}(0) - k_{-1}\boldsymbol{\rho}_{DD}(t) - \frac{i}{\hbar}[\boldsymbol{H_{DD}}, \boldsymbol{\rho}_{DD}(t)] - \frac{k_S}{2}\left(\boldsymbol{\rho}_{DD}(t)\boldsymbol{\Lambda}_S + \boldsymbol{\Lambda}_S\boldsymbol{\rho}_{DD}(t)\right) - \frac{k_T}{2}\left(\boldsymbol{\rho}_{DD}(t)\boldsymbol{\Lambda}_T + \boldsymbol{\Lambda}_T\boldsymbol{\rho}_{DD}(t)\right), \quad \text{(S2)}$$

where

$$\boldsymbol{H_{DD}} = g_{D1}\mu_B\boldsymbol{B}\cdot\boldsymbol{S_{D1}} + g_{D2}\mu_B\boldsymbol{B}\cdot\boldsymbol{S_{D2}} + \boldsymbol{S^T}\cdot\boldsymbol{D}\cdot\boldsymbol{S^T} + \sum_i \boldsymbol{S_{D1}}\cdot\boldsymbol{A_i}\cdot\boldsymbol{I_{D1i}} + \sum_j \boldsymbol{S_{D2}}\cdot\boldsymbol{A_j}\cdot\boldsymbol{I_{D2j}} - 2J\boldsymbol{S_{D1}}\cdot\boldsymbol{S_{D2}}, \quad \text{(S3)}$$

and

$$\boldsymbol{\Lambda}_S = |S><S| \quad \text{(S4)}$$

$$\boldsymbol{\Lambda}_T = \textstyle\sum_i |T_i><T_i| \quad \text{(in the eigenfunction basis of } \boldsymbol{S}^2 \text{ operator)} \quad \text{(S5)}$$

in which (S2) and (S3) are the same as eqn (5) and (6) in the main text. Here, $\boldsymbol{\rho}_{DD}(t)$ is the density matrix of the DD pair at time *t*. $\boldsymbol{\rho}_{DD}(0)$ is the initial conditions at time zero, in which the spin-doublet electron and hole carrier are just encountered. k_1, k_{-1}, k_S and k_T are the rate constants for the each process depicted in the Scheme S1. $\boldsymbol{H_{DD}}$ is the effective spin-Hamiltonian for the DD model. The first and second terms in eqn (S3) are the electron Zeeman terms of the two doublet species (electron and hole carriers), respectively. The third term in eqn (S3) is the fine-structure term of the triplet state arising from the spin-exchange coupling between the electron and hole carriers. The fourth and fifth terms are the hyperfine interactions within the each doublet carriers. The last term is the exchange interaction between the doublet species. $\boldsymbol{\Lambda}_S$ and $\boldsymbol{\Lambda}_T$ are the projection operators to the doublet states and the triplet states. We have assumed the selective population to the singlet pair ($^1(^2$e–^{2}h)) as the initial conditions of the density matrix at the time zero ($\boldsymbol{\rho}_{DD}(0)$), because the charge separated singlet excited states ($^1(D^+ - A^-)$) is effectively generated by the direct photoexcitation of the CT band in such weak CT complex. In the calculation, we have chosen the weak coupled (WC) basis which is written as $|S_{D1}, m_{D1}> |S_{D2}, m_{D2}>$. The initial density matrix, $\boldsymbol{\rho}_{DD}(0)$, is given by

$$\boldsymbol{\rho}_{DD}(0) = |S><S| = U_{S(S+1)\to WC}\begin{pmatrix}0&0&0&0\\0&0&0&0\\0&0&1&0\\0&0&0&0\end{pmatrix}U^{+}_{S(S+1)\to WC}, \quad \text{(S6)}$$

$U_{S(S+1)\to WC}$ is the unitary transformation matrix from the eigenfunction basis of $\boldsymbol{S}^2$ operator to the WC basis. The rate equation of (S2) was rewritten in the Löuville space as follows.

$$\frac{\mathrm{d}}{\mathrm{d}t}\boldsymbol{\rho}_{DD}^{L}(t) = k_1\boldsymbol{\rho}_{DD}^{L}(0) - \boldsymbol{L}_{DD}\boldsymbol{\rho}_{DD}^{L}(t)\,, \tag{S7}$$

where

$$\boldsymbol{\rho}_{DD}^{L}(t) = \begin{pmatrix} \rho(t)_{11} \\ \rho(t)_{12} \\ \vdots \end{pmatrix}\,, \tag{S8}$$

and

$$\boldsymbol{L_{DD}}(t) = k_{-1}\boldsymbol{E}\otimes\boldsymbol{E} + \frac{i}{\hbar}(\boldsymbol{H_{DD}}\otimes\boldsymbol{E} - \boldsymbol{E}\otimes\boldsymbol{H_{DD}^{*}}) + \frac{k_S}{2}(\boldsymbol{\Lambda_S}\otimes\boldsymbol{E} + \boldsymbol{E}\otimes\boldsymbol{\Lambda_S^{*}}) + \frac{k_T}{2}(\boldsymbol{\Lambda_T}\otimes\boldsymbol{E} + \boldsymbol{E}\otimes\boldsymbol{\Lambda_T^{*}})\,. \tag{S9}$$

Here, $\boldsymbol{E}$ is the unit matrix. In the steady-state approximation of $d\boldsymbol{\rho}_{DD}(t)/dt$ =0, the solution of the density matrix is easily solved as follows.

$$\boldsymbol{\rho}_{DD}^{L} = k_1\boldsymbol{L_{DD}^{-1}}\boldsymbol{\rho}_{DD}^{L}(0)\,, \tag{S10}$$

The efficiency of the charge-separation yield, in which the external magnetic field is applied to the (θ, ϕ) direction to the principal axes (X, Y, Z) of the fine-structure tensor, can be calculated as follows.

$$\emptyset_{\mathrm{DD}}(B,\theta,\phi) = (k_{-1}/k_1)Tr(\boldsymbol{\rho}_{DD}\boldsymbol{E}) = (k_{-1}/k_1)Tr(\boldsymbol{\rho}_{DD}). \tag{S11}$$

Since the molecules are oriented randomly in the sample, the averaged MC effect is given by

$$\langle\emptyset_{\mathrm{DD}}(B)\rangle = \frac{1}{4\pi}\int_0^{2\pi}\int_0^{\pi}\emptyset_{\mathrm{DD}}(B,\theta,\phi)\sin\theta\,\mathrm{d}\theta d\phi \tag{S12}$$

The MC effect arising from the DD mechanism in the photocurrent is given by

$$\mathrm{MC} = \frac{\langle\emptyset_{\mathrm{DD}}(B)\rangle - \langle\emptyset_{\mathrm{DD}}(0)\rangle}{\langle\emptyset_{\mathrm{DD}}(0)\rangle}\mathrm{x}100\quad. \tag{S13}$$

In the simulation, the summation of the hyperfine tensors in eqn (S3) was approximated by the effective isotropic hyperfine-couplings as follows.

$$\begin{aligned}\boldsymbol{H_{DD}} = {} & g_{D1}\mu_B\boldsymbol{B}\cdot\boldsymbol{S_{D1}} + g_{D2}\mu_B\boldsymbol{B}\cdot\boldsymbol{S_{D2}} + \boldsymbol{S^T}\cdot\boldsymbol{D}\cdot\boldsymbol{S^T} \\ & + \boldsymbol{a_{D1}^{eff}}\boldsymbol{S_{D1}}\cdot\boldsymbol{I_{D1}} + \boldsymbol{a_{D2}^{eff}}\boldsymbol{S_{D2}}\cdot\boldsymbol{I_{D2}} - 2J\boldsymbol{S_{D1}}\cdot\boldsymbol{S_{D2}}\,,\end{aligned} \tag{S14}$$

The effective isotropic hyperfine-couplings of the cation radical of pyrene and the anion radical of DMPI were estimated to be $\boldsymbol{a_{D1}^{eff}}$ = −30.0 MHz and $\boldsymbol{a_{D2}^{eff}}$ = −8.0 MHz, respectively, as described in Sec. S7. It should be noted that the closest contact e-h pair within the CT complex ($\mathrm{D}^+ - \mathrm{A}^-$) could not contribute to the MC effect, because of the large energy splitting between the singlet ($^1(\mathrm{D}^+ - \mathrm{A}^-)$) and triplet ($^3(\mathrm{D}^+ - \mathrm{A}^-)$) states induced by the large exchange coupling. Therefore, in the simulation of the DD pair mechanism, we used the estimated D value (– 0.00782 cm^{-1}) of the second nearest contact between D and A, which was calculated by eqn (2) using the distance (6.937 Å) obtained by the X ray crystallographic structure (see Fig. S5). The second, third closest, or fourth contact e-h pairs will contribute to the MC effects as discussed in the literatures.[S1, S2] The following stepwise electron or hole hopping model is better one, which is close to the actual situation of the present system.

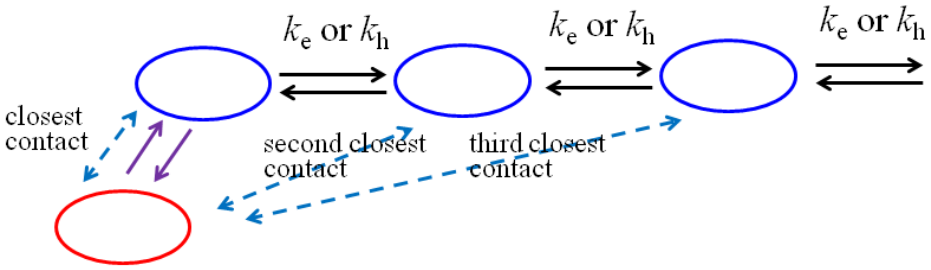

Fig. S11 Stepwise electron or hole hopping model.

However, to discuss the shape of the MC curve, only choice of the second closest contact pair is enough. Since there are some estimated or unknown parameters, such as the absolute value of the rate constants, definite discussion of the magnitude of the MC effect is difficult. Therefore, we discuss the MC effect in the DD mechanism using that of the second closest contact e-h pair. In the actual MC effect measurement, the lowest magnetic field was 3 mT, because of the residual magnetization of the iron core magnet used. Therefore, in the simulation shown in Fig.6, we used $\langle \emptyset_{\mathrm{DD}}(3\,mT) \rangle$ instead of $\langle \emptyset_{\mathrm{DD}}(0) \rangle$ in eqn (S13). Further discussions using the stepwise electron or hole hopping model and the extreme low-field and anisotropy measurements using air-core magnet are planned and in progress. Here, we present the results using $\langle \emptyset_{\mathrm{DD}}(0) \rangle$ as well as the results using $\langle \emptyset_{\mathrm{DD}}(3\,mT) \rangle$ instead of $\langle \emptyset_{\mathrm{DD}}(0) \rangle$ in eqn (S13). The selective population to the singlet pair ($^1(^2\mathrm{e}\text{–}^2\mathrm{h})$) was assumed as the initial conditions of the density matrix ($\boldsymbol{\rho}_{DD}(0)$), because the charge separated singlet excited states ($^1(\mathrm{D}^+ - \mathrm{A}^-)$) is effectively generated by the direct photoexcitation of the CT band in such weak CT complex. The results in the limited condition of J = 0 cm^{-1} are given in Fig. 6(b). Fig. S12 shows the typical J dependence of the MC curves. As shown here, the MC curves similar to the observed one are expected only for the small J values.

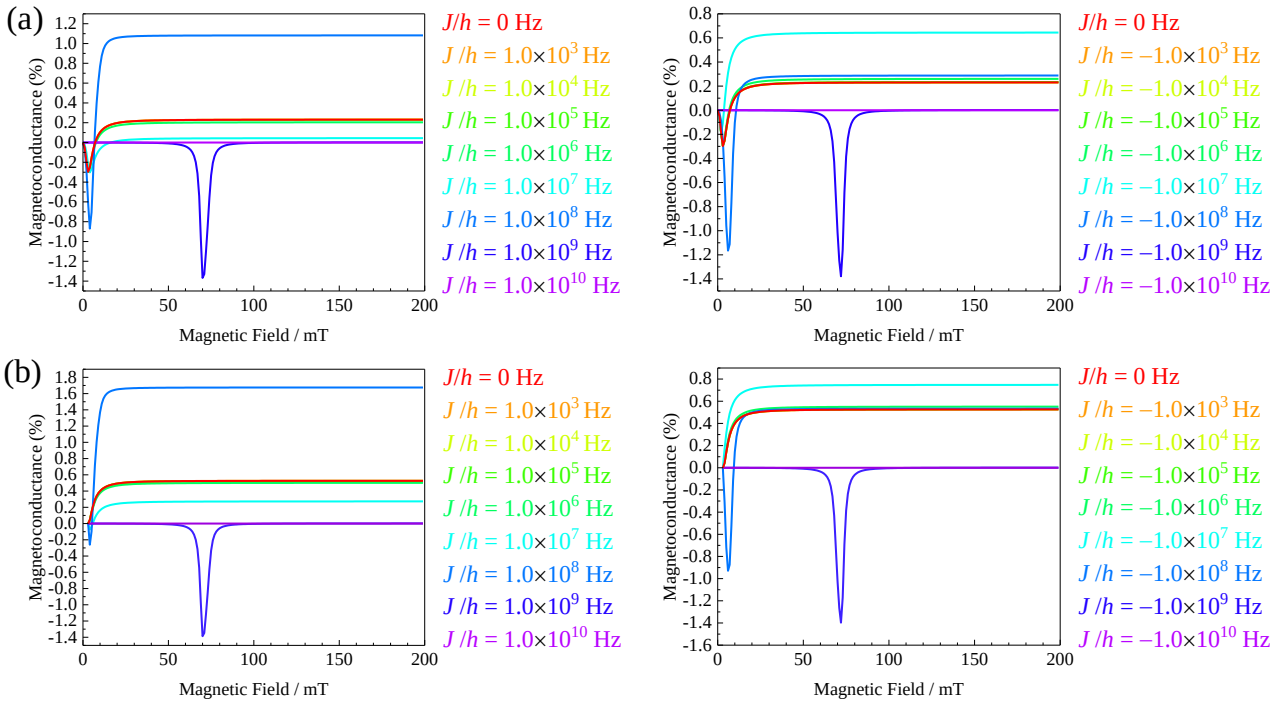

Fig.S12 J dependence of the MC curves (g_{D1} = 2.0030, g_{D2} = 2.0030, D = −0.00782 cm^{-1}, E = 0.0 cm^{-1}, $\boldsymbol{a}_{\boldsymbol{D1}}^{\boldsymbol{eff}}$ = −30.0 MHz, $\boldsymbol{a}_{\boldsymbol{D2}}^{\boldsymbol{eff}}$ = −8.0 MHz, $k_1 = k_{-1}$ = 1.0×10^8 s^{-1}, k_S = 1.0×10^8 s^{-1} and k_T = 1.7×10^8 s^{-1}). (a) The result using eqn (S13). (b) The result using $\langle \emptyset_{\mathrm{DD}}(3\,mT) \rangle$ instead of $\langle \emptyset_{\mathrm{DD}}(0) \rangle$ in eqn (S13).

We also checked the k dependence of the MC curves. The results are shown in Figs. S13 – 15.

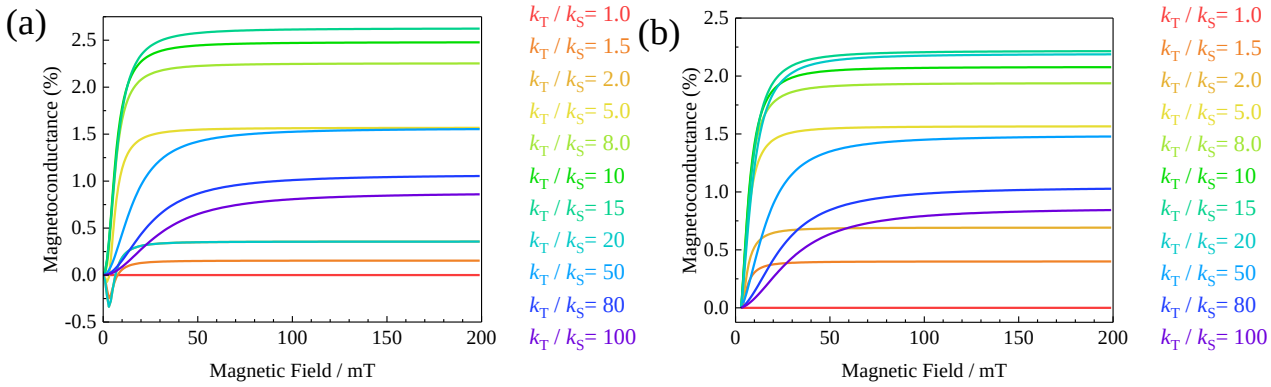

Fig.S13 k_T dependence of the MC curves (g_{D1} = 2.0030, g_{D2} = 2.0030, D = −0.00782 cm^{-1}, E = 0.0 cm^{-1}, $\boldsymbol{a}_{\boldsymbol{D1}}^{\boldsymbol{eff}}$ = −30.0 MHz, $\boldsymbol{a}_{\boldsymbol{D2}}^{\boldsymbol{eff}}$ = −8.0 MHz, $k_1 = k_{-1}$ = 1.0×10^8 s^{-1}, k_S = 1.0×10^8 s^{-1}, and J = 0 cm^{-1}). (a) The result using eqn (S13). (b) The result using $\langle \emptyset_{\mathrm{DD}}(3\,mT) \rangle$ instead of $\langle \emptyset_{\mathrm{DD}}(0) \rangle$ in eqn (S13).

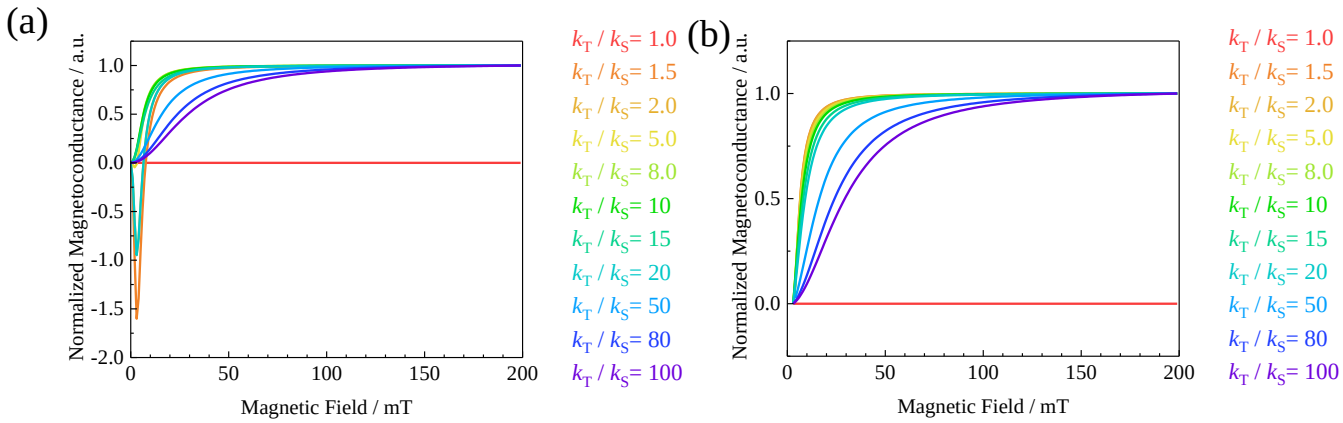

Fig.S14 k_T dependence of the MC curves normalized by the value at 200 mT (g_{D1} = 2.0030, g_{D2} = 2.0030, D = −0.00782 cm^{-1}, E = 0.0 cm^{-1}, $\boldsymbol{a}_{D1}^{eff}$ = −30.0 MHz, $\boldsymbol{a}_{D2}^{eff}$ = −8.0Hz, k_1 = k_{-1} = 1.0×10^8 s^{-1}, k_S = 1.0×10^8 s^{-1}, and J = 0 cm^{-1}). (a) The result using eqn (S13). (b) The result using $\langle \emptyset_{DD}(3\,mT) \rangle$ instead of $\langle \emptyset_{DD}(0) \rangle$ in eqn (S13).

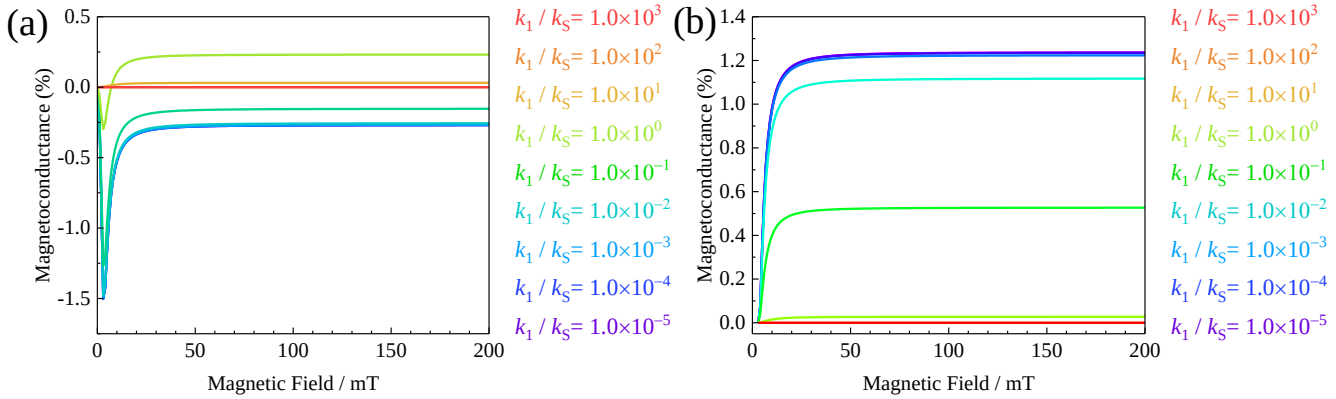

Fig.S15 k_1 dependence of the MC curves (g_{D1} = 2.0030, g_{D2} = 2.0030, D = −0.00782 cm^{-1}, E = 0.0 cm^{-1}, $\boldsymbol{a}_{D1}^{eff}$ = −30.0 MHz, $\boldsymbol{a}_{D2}^{eff}$ = −8.0 MHz, k_1 = k_{-1}, k_S = 1.0×10^8 s^{-1}, k_T = 1.7×10^8 s^{-1}, and J = 0 cm^{-1}). (a) The result using eqn (S13). (b) The result using $\langle \emptyset_{DD}(3\,mT) \rangle$ instead of $\langle \emptyset_{DD}(0) \rangle$ in eqn (S13).

The presence of the fine-structure term leads to the internal field even in the zero external magnetic field. In such a case, $\langle \emptyset_{DD}(0) \rangle < \langle \emptyset_{DD}(B) \rangle$ occurs sometimes by the internal field. However, since $\langle \emptyset_{DD}(3\text{ mT}) \rangle > \langle \emptyset_{DD}(B) \rangle$ in the region of B > 3 mT, the apparent positive MC effect were always obtained, when we used $\langle \emptyset_{DD}(3\,mT) \rangle$ instead of $\langle \emptyset_{DD}(0) \rangle$ in eqn (S13).

References

S1. F. Ito, T. Ikoma, K. Akiyama, Y. Kobiri, S. Tero-Kubota, *J. Am. Chem. Soc.*, 2003, 125, 4722-4723.
S2. M. Wakasa, M. Kaise, T.Yago, R. Katoh, Y. Wakikawa, T. Ikoma, *J. Phys. Chem. C* 2015, 119, 25840-25844.

S11. Detail procedures of the MC effect calculation by the TD pair mechanism and the *J* and *k* dependences

The kinetic models of the TD mechanism is given in Scheme S2, which are similar to used for the analyses of the MC effects of pentacene/C60 bi-layer solar cell by Ikoma et al (ref. [19] in the main text).

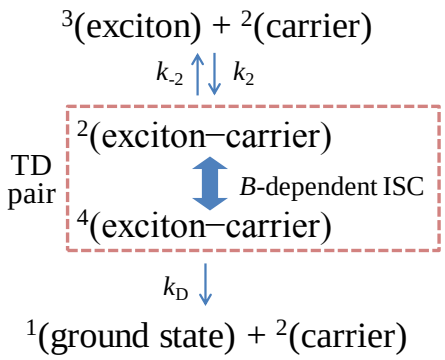

Scheme S2 A kinetic models of the TD mechanism

The rate equation of the density matrix for the TD mechanism is given by

$$\frac{\mathrm{d}\boldsymbol{\rho}_{TD}(t)}{\mathrm{d}t} = k_2\boldsymbol{\rho}_{TD}(0) - k_{-2}\boldsymbol{\rho}_{TD}(t) - \frac{i}{\hbar}[\boldsymbol{H_{TD}}, \boldsymbol{\rho}_{TD}(t)] - \frac{k_D}{2}\left(\boldsymbol{\rho}_{TD}(t)\boldsymbol{\Lambda}_D + \boldsymbol{\Lambda}_D\boldsymbol{\rho}_{TD}(t)\right), \qquad \text{(S14)}$$

where

$$\boldsymbol{H_{TD}} = g_D\mu_B\boldsymbol{B}\cdot\boldsymbol{S_D} + g_T\mu_B\boldsymbol{B}\cdot\boldsymbol{S_T} + \boldsymbol{S_T}\cdot\boldsymbol{D_T}\cdot\boldsymbol{S_T} - 2J\boldsymbol{S_D}\cdot\boldsymbol{S_T}, \qquad \text{(S15)}$$

and

$$\boldsymbol{\Lambda}_D = \sum_i |D_i><D_i| \qquad \text{(in the eigenfunction basis of } \boldsymbol{S}^2 \text{ operator)} \qquad \text{(S16)}$$

in which (S14) and (S15) are the same as eqn (8) and (9) in the main text. Here, $\boldsymbol{\rho}_{\mathrm{TD}}(t)$ is the density matrix of the TD pair at time *t*. $\boldsymbol{\rho}_{\mathrm{TD}}(0)$ is the initial conditions at time zero, when the triplet species and doublet carrier are just encountered. k_2, k_{-2}, and k_{D} are the rate constants for the each process depicted in the Scheme S2. $\boldsymbol{H}_{\mathbf{TD}}$ is the effective spin-Hamiltonian for TD model. The first and second terms in eqn (S15) are the electron Zeeman terms of the doublet and triplet species, respectively. The third and forth terms in eqn (S15) are the fine-structure term of the triplet species and the exchange interaction between the doublet species and the triplet species. $\boldsymbol{\Lambda}_D$ is the projection operator to the doublet states. We have assumed that the dynamic electron spin polarization (DESP) observed in the TRESR experiment is kept at the time zero. In the calculation, we have chosen the weak spin-coupled (WC) basis which is written as $|S_{\mathrm{D}}, m_{\mathrm{D}}> |S_{\mathrm{T}}, m_{\mathrm{T}}>$. The initial density matrix, $\boldsymbol{\rho}_{\mathrm{TD}}(0)$, is given by

$$\boldsymbol{\rho}_{TD}(0)=\boldsymbol{\rho}_D(0)\otimes\boldsymbol{\rho}_T(0). \qquad \text{(S17)}$$

Here,

$$\boldsymbol{\rho}_D(0) = \begin{pmatrix} 1/2 & 0 \\ 0 & 1/2 \end{pmatrix}, \qquad \boldsymbol{\rho}_T(0) = U_{ZF\to WC}\begin{pmatrix} P_{\mathrm{X}} & 0 & 0 \\ 0 & P_{\mathrm{Y}} & 0 \\ 0 & 0 & P_{\mathrm{Z}} \end{pmatrix}_{ZF} U^{+}_{ZF\to WC} \qquad \text{(S18)}$$

$U_{ZF\to WC}$ is the unitary transformation matrix from the zero-field eigenfunction basis to the WC basis, which is obtained by the diagonalization of $\boldsymbol{H_{Zf}} = \boldsymbol{S_T}\cdot\boldsymbol{D_T}\cdot\boldsymbol{S_T}$. The rate equation of (S14) was rewritten in the Löuville space as follows.

$$\frac{\mathrm{d}}{\mathrm{d}t}\boldsymbol{\rho}^L_{TD}(t) = k_2\boldsymbol{\rho}^L_{TD}(0) - \boldsymbol{L}_{TD}\boldsymbol{\rho}^L_{TD}(t), \qquad \text{(S19)}$$

where

$$\boldsymbol{\rho}_{TD}^{L}(t) = \begin{pmatrix} \rho(t)_{11} \\ \rho(t)_{12} \\ \vdots \end{pmatrix} , \tag{S20}$$

and

$$\boldsymbol{L_{TD}}(t) = k_{-2}\boldsymbol{E}\otimes\boldsymbol{E} + \frac{i}{\hbar}(\boldsymbol{H_{TD}}\otimes\boldsymbol{E} - \boldsymbol{E}\otimes\boldsymbol{H}_{\boldsymbol{TD}}^{*}) + \frac{k_D}{2}\left(\boldsymbol{\Lambda_D}\otimes\boldsymbol{E} + \boldsymbol{E}\otimes\boldsymbol{\Lambda_D}\right) \quad . \tag{S21}$$

Here, $\boldsymbol{E}$ is the unit matrix in the spin-space of the TD pair. In the steady-state approximation of $d\boldsymbol{\rho}_{TD}(t)/dt = 0$, the solution of the density matrix is easily solved as follows.

$$\boldsymbol{\rho}_{TD}^{L} = k_2\boldsymbol{L}_{\boldsymbol{TD}}^{-\boldsymbol{1}}\boldsymbol{\rho}_{TD}^{L}(0) , \tag{S22}$$

In the carrier trapping case on the TD pair mechanism, the return (release) pathway (k_{-2}) of the mobile carrier (^2c) from the collision pair leads to the photocurrent. The efficiency at the (θ, ϕ) direction of the external magnetic field to the principal axes (X, Y, Z) of the fine-structure tensor, $\boldsymbol{D}$, is given by

$$\emptyset_{\mathrm{TD}}(B,\theta,\phi) = (k_{-2}/k_2)Tr(\boldsymbol{\rho}_{TD}\boldsymbol{E}) = (k_{-2}/k_2)Tr(\boldsymbol{\rho}_{TD}) \quad . \tag{S23}$$

In the carrier detrapping case on the TD pair mechanism, the forward (detrapping) pathway (k_{D}) of the mobile carrier (^2c) from the collision pair leads to the photocurrent. The efficiency at the (θ, ϕ) direction of the external magnetic field to the principal axes (X, Y, Z) of the fine-structure tensor, $\boldsymbol{D}$, is given by

$$\emptyset_{\mathrm{TD}}(B,\theta,\phi) = (k_D/k_2)Tr(\boldsymbol{\rho}_{TD}\boldsymbol{\Lambda}_D) \quad . \tag{S24}$$

Since the molecules are oriented randomly in the sample, the averaged MC effect is given by

$$\langle\emptyset_{\mathrm{TD}}(B)\rangle = \frac{1}{4\pi}\int_0^{2\pi}\int_0^{\pi}\emptyset_{\mathrm{TD}}(B,\theta,\phi)\sin\theta\,\mathrm{d}\theta d\phi \tag{S25}$$

The MC effect arising from the TD mechanism in the photocurrent is given by

$$\mathrm{MC} = \frac{\langle\emptyset(B)\rangle_{\mathrm{TD}} - \langle\emptyset(0)\rangle_{\mathrm{TD}}}{\langle\emptyset(0)\rangle_{\mathrm{TD}}}\mathrm{x}100 \tag{S26}$$

In the actual MC effect measurement, the lowest magnetic field was 3 mT, because of the residual magnetization of the iron core magnet used. Therefore, in the simulation shown in Fig.6, we used $\langle\emptyset_{\mathrm{TD}}(3\,mT)\rangle$ instead of $\langle\emptyset_{\mathrm{TD}}(0)\rangle$ in eqn (S26). Here, we present the results using $\langle\emptyset_{\mathrm{TD}}(0)\rangle$. The results in the limited condition of J = 0 cm^{-1} are given in Fig. 6(b) in the main text. Fig. S16 shows the typical J dependence of the MC curves. As shown here, the MC curves similar to the observed one are expected only for the small J values.

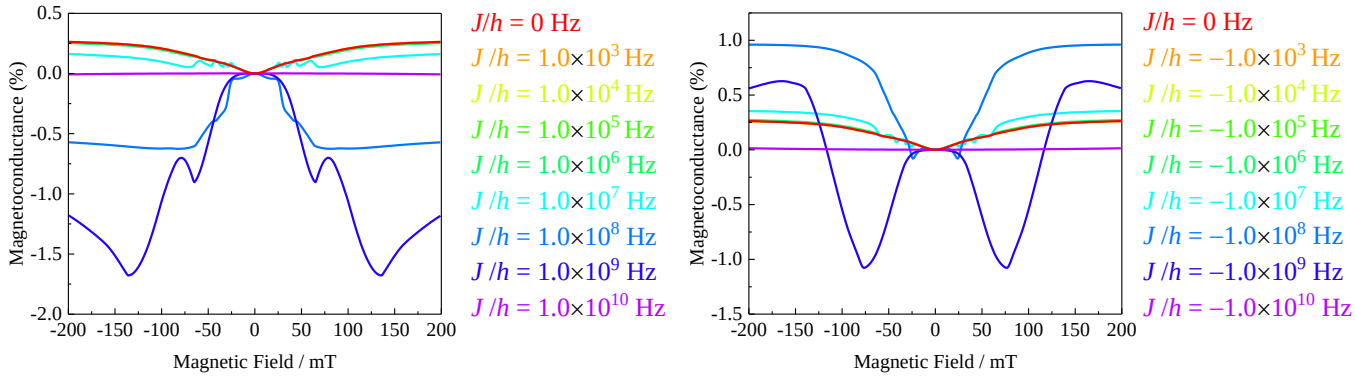

Fig.S16 J dependence of the MC curves. (g_T = 2.0050, g_D = 2.0023, $|D|$ = 0.0830 cm^{-1}, $|E|$ = 0.0160 cm^{-1} Px = 0.00, Py = 0.92, Pz = 0.08, k_2 = k_{-2} = 1.0×10^8 s^{-1}, and k_{D} = 2.0×10^7 s^{-1})

We also checked the k dependence of the MC curves. The results are shown in Figs. S17 and S18.

When only the k_2 was change and other parameters were fixed, no deference was observed shown in Fig. S17.

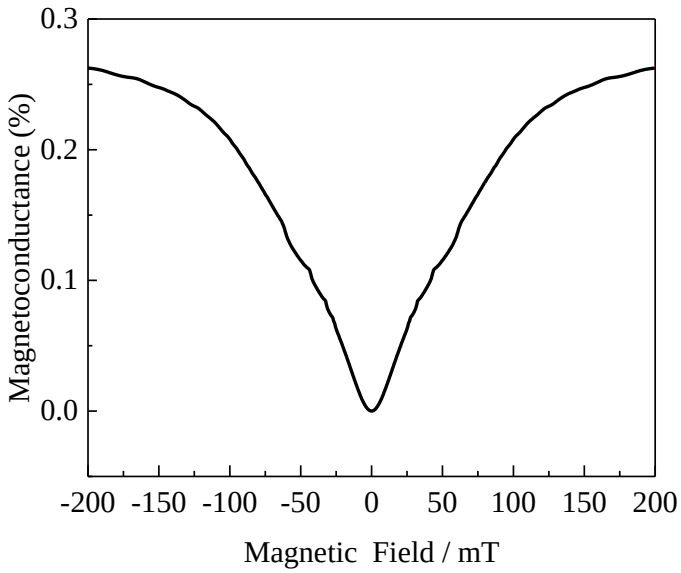

Fig.S17 k_2 dependence of the MC curves. (g_T = 2.0050, g_D = 2.0023, $|D|$ = 0.0830 cm^{-1}, $|E|$ = 0.0160 cm^{-1} Px = 0.00, Py = 0.92, Pz = 0.08, k_{-2} = 1.0×10^8 s^{-1}, k_D = 2.0×10^7 s^{-1}, and J = 0 cm^{-1}). k_2 was changed from 1.0×10^{12} s^{-1} to 1.0×10^{12} s^{-1}. No deference was observed.

When the k_D was change and k-$_2$, and other parameters were fixed, deference was observed depending on the ratio, k_D /k_2 or k_D /k-$_2$, as shown in Fig. S18.Very large MC effect (> 500 %) was expected when k_D/k_2 = 100.

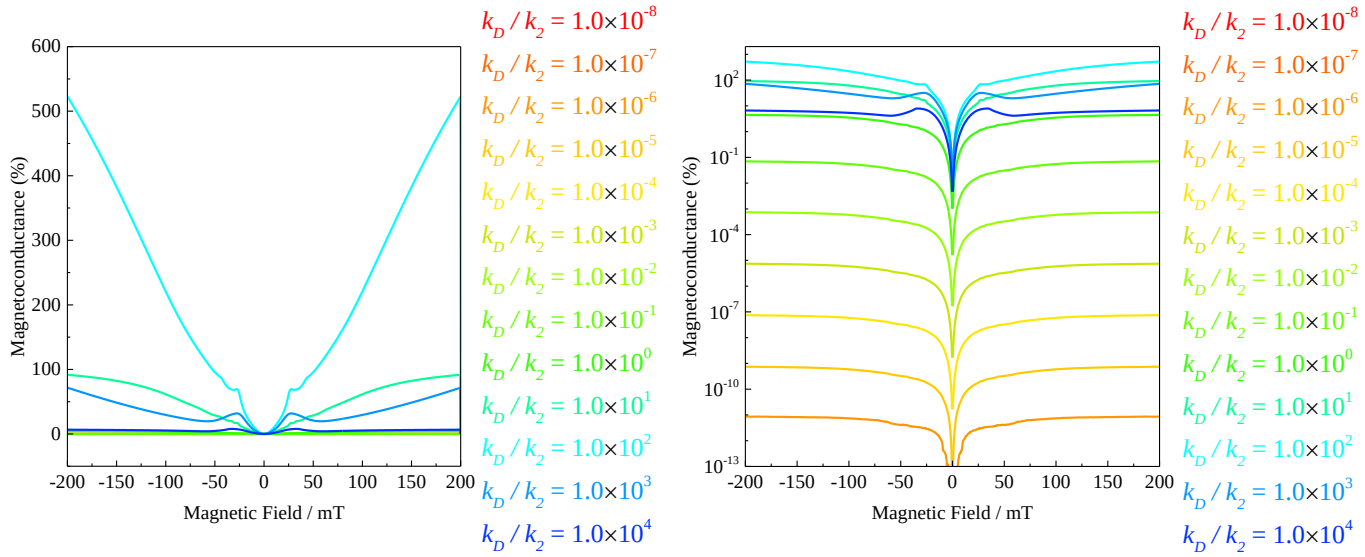

Fig.S18 $k_D$dependence of the MC curves. (g_T = 2.0050, g_D = 2.0023, $|D|$ = 0.0830 cm^{-1}, $|E|$ = 0.0160 cm^{-1} Px = 0.00, Py = 0.92, Pz = 0.08, k_2 = k_{-2} = 1.0×10^8 s^{-1}, and J = 0 cm^{-1})